Magnonic Interconnections: Spin-Wave Propagation across Two-Dimensional and Three-Dimensional Junctions between Yttrium Iron Garnet Magnonic Stripes

A.A. Martyshkin[ORCID],[1] C.S. Davies,[2] and A.V. Sadovnikov[ORCID][1,*]

[1]*Saratov State University, Laboratory "Magnetic Metamaterials", Saratov 410012, Russia*
[2]*FELIX Laboratory, Radboud University, Toernooiveld 7 Nijmegen 6525 ED, Netherlands*

Spin-wave transport across multidimensional networks of magnonic waveguides represents a crucial and necessary aspect of prospective densely packed three-dimensional spin-wave architectures. Here, we report the results of investigations of spin-wave propagation through magnonic waveguides extending along and bending across two and three dimensions. We consider three designs of in-plane two-dimensional bends, namely with right-angled, diagonal, and curved geometries. Our numerical and experimental results show that such bends facilitate the conversion of spin-wave types, with the output modal number depending on the spin-wave frequency. At the same time, variation of the width of lateral magnonic bends enables the spin-wave wavelength to be modified. When propagating across three-dimensional waveguide bends in the form of out-of-plane junctions, the spin-wave wavelength can similarly be tuned by adjusting the stripe's thickness. Our results show that magnonic waveguides can serve not only as passive conduits but also as active elements in modifying the properties of the transmitted spin wave in three-dimensional magnonic networks.

I. INTRODUCTION

Recent years have witnessed a rapid rise in the number and variety of studies of mechanisms and methods of the excitation and control of spin waves (SWs) in magnetic materials [1–3]. In particular, advances in the technology of thin-film patterning have enabled a wide use of micro- and nanostructures to create magnonic devices. When combined into multielement magnonic networks (MNs) [4,5], such devices are interconnected by magnonic waveguides, carrying signals encoded into the spin-wave amplitude and/or phase [6–8]. Analogous to CMOS-based circuitry [9,10], MNs of functional elements can be used to achieve logic-gate functionality [6,11–13], enabling, e.g., NOT, XOR, NOR, AND, and NAND gates to route and process information. Compared to electrical currents, the use of SWs for such operations provide the additional benefits of nonvolatility, low operational power, and reduced Joule heating [14–19].

The damping of SWs poses a critical obstacle for the creation of MNs, by limiting their spatial extent to scales comparable or smaller to the SW's propagation length. Record low damping rates can be achieved when using films of yttrium iron garnet (YIG) that allow spin waves to propagate across distances of up to several millimeters [16,20]. Yet, the micrometer wavelengths of such SWs is

in itself an obstacle for device miniaturization, urging us to search for concepts that would be more easily downscaled.

A possible solution lies in expanding MNs into the third dimension [21], beyond the conventionally studied planar geometries. This would allow one both to reduce the footprint of individual SW devices and to shorten the magnonic interconnects between them, thereby increasing the element density without producing excess heat. The latter is a major problem, well known, e.g., for three-dimensional (3D) CMOS-based circuitry [22]. Moreover, the possibility of setting or reading the state of magnetization using current driven wires [23], magnetic tunnel junctions [24], or YIG/GaAs structures [16,25] provides for interfacing between magnonic and CMOS technologies. However, as with other magnetic logic concepts [15], the use of three-dimensional MNs hinges on efficiently routing the SW signal from one functional level to another. Hence, it is worthwhile to study mechanisms associated with SW transport in multilevel topologies of MNs based on three-dimensional structures.

Recently the concept of using 3D magnonic structures was explored in magnonic crystals fabricated using nanometer-thick meander-shaped $Co_{40}Fe_{40}B_{20}$ [26,27], $Ni_{80}Fe_{20}$ [28], and YIG [29,30] films consisting of ferromagnetic segments arranged at 90° angles with respect to each other. Compared to conventional magnonic crystals extending along one axis, such meandering geometries have the advantage of potentially overcoming the

---

*SadovnikovAV@gmail.com

　　　　　064093-1

limitations of spin-wave manipulation and steering in in-plane magnetized films arising from the anisotropic spin-wave dispersion, while also allowing for SW propagation in three dimensions without significant losses in the junction region. The latter raises a question of whether spin waves can be transmitted across significantly longer distances across the meandering structures. To connect the magnonic building blocks with each other, junctions in both the lateral (in-plane) and out-of-plane directions must be introduced. Such bends break the translational symmetry of the conventional magnonic waveguide. So, it is worthwhile to study the effect of this symmetry breaking on spin-wave propagation in such junctions, within both in-plane [31–35] and out-of-plane [26,27,29] geometries.

In this paper, using numerical and experimental methods we study a variant of the implementation of interlevel SW transport between parallel layers of MNs based on orthogonally connected magnonic waveguides. We reveal peculiarities of SW signal-routing through waveguide junctions (bends) of different configurations. The proposed element for interconnecting the functional levels of MNs allows one to implement the functions of a frequency filter and wavelength converter.

The paper is divided into sections as follows. Firstly, we describe the geometrical and fabrication details of the different types of magnonic bends. Secondly, we describe the numerical and experimental methods used to characterize the spin-wave propagation across the magnonic waveguides with broken translational symmetry. Thirdly, we discuss the results of this investigation, concentrating on each structure in turn. Fourthly and finally, we present our conclusions.

II. 2D AND 3D MAGNONIC BENDS: DESCRIPTION AND FABRICATION

The sequential orthogonal connection of three rectangular magnetic stripes, labeled as "A", "B", and "C" in Fig. 1(a), represents a generic three-dimensional magnonic

waveguide, called ABC, with translation symmetry broken both in the horizontal and vertical planes. We refer to continuous translational symmetry in a particular direction (e.g., x, y, or z) as invariance of a waveguide's cross section in the plane orthogonal to that direction. To study systematically the propagation of SWs across this structure in a bottom-up approach, we deconstruct the 3D waveguide into its elementary parts. The first part $A_P B_P$ represents a lateral magnonic bend in the x-y plane [Fig. 1(b)], formed itself of two stripes A_P and B_P. The second part $B_V C_V$ represents a vertical magnonic bend in the y-z plane [Fig. 1(c)], comprising the stripes B_V and C_V. Note that we use subscripts "P" and "V" to denote stripes comprising the in-plane and out-of-plane bends, respectively.

For our measurements, the waveguide junction $A_P B_P$ is fabricated from 10-μm-thick single-crystal YIG films [$Y_3Fe_2(FeO_4)_3$ (111)] [36] with saturation magnetization $4\pi M_s = 1750$ G grown epitaxially on gadolinium gallium garnet substrates [GGG, $Gd_3Ga_5O_{12}$ (111)]. The linewidth of the ferromagnetic resonance for YIG is 0.5 Oe. The films are patterned using a local laser ablation system (LLAS) based on a Nd:YAG fiber laser with a two-dimensional (2D) galvanometric scanning module (Cambridge Technology 6240H) operating in a pulsed regime with a pulse duration of 50 ns and energy of 50 mJ. The width of the YIG waveguides is $w = 500$ μm throughout. Section lengths are labeled as l_n, where $n = 1, 2, 3$ is the section number in Fig. 1. Three different types of in-plane waveguide bends are fabricated: a rounded bend (W_1), a sharp corner (W_2), and a diagonal 45° connection (W_3).

The considered $B_V C_V$ structure is formed by attaching two 1-mm-wide and 10-μm-thick YIG stripes B_V and C_V orthogonally to each other, as shown in Fig. 1(c).

III. METHODS

A. Micromagnetic modeling

The SW propagation across the different structures is modeled using the micromagnetic software MuMax3 [37],
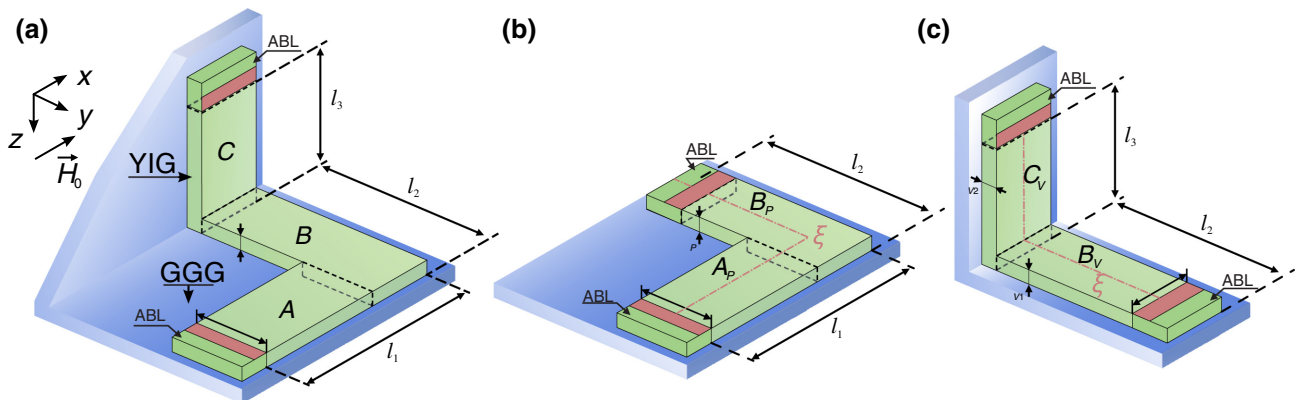

FIG. 1. (a) Schematic of the three-dimensional ABC waveguide structure. (b),(c) Schematic of the two-dimensional in-plane ($A_P B_P$, extending across the x-y plane) and out-of-plane ($B_V C_V$, extending across the y-z plane) junctions, respectively.

based on numerically solving the Landau-Lifshitz-Gilbert (LLG) equation [38–41]:

$$\frac{\partial \mathbf{M}}{\partial t} = \gamma[\mathbf{H}_{\text{eff}} \times \mathbf{M}] + \frac{\alpha}{M_s}\left[\mathbf{M} \times \frac{\partial \mathbf{M}}{\partial t}\right], \quad (1)$$

which describes the precession of the magnetization vector $\mathbf{M}$ in the effective magnetic field $\mathbf{H}_{\text{eff}} = \mathbf{H}_0 + \mathbf{H}_{\text{demag}} + \mathbf{H}_{\text{ex}} + \mathbf{H}_a$, where $\mathbf{H}_0$ is the external magnetic field, $\mathbf{H}_{\text{demag}}$ the demagnetizing field, $\mathbf{H}_{\text{ex}}$ the exchange field, and $\mathbf{H}_a$ the anisotropy field. The micromagnetic calculations allow one to numerically solve the problem of the excitation and propagation of spin waves in an irregular magnetic microstructure [35,42,43].

We assume that the YIG's magnetocrystalline anisotropy is negligible relative to the shape anisotropy, and so $\mathbf{H}_a = 0$. The shape anisotropy is well understood to play a crucial role in the spin-wave transport along the magnonic bend [35]. The exchange constant for YIG is $A_{\text{ex}} = 3\times10^{-7}$ erg/cm, and the damping parameter is set to $\alpha = 10^{-5}$. To reduce SW reflections from the boundaries of the computational domain, we introduce absorbing boundary layers (ABL) with an exponentially decreasing attenuation coefficient α at the beginning of the input and at the end of the output sections of the waveguide structure [44]. The sources of excitation and detection of the spin-wave signal are located immediately adjacent to the ABL regions at the ends of the waveguides [45], as shown by the red areas for each structure in Fig. 1. Thin YIG films exhibit three types of magnetostatic spin waves, namely magnetostatic surface spin waves (MSSWs), forward volume magnetostatic spin waves (FVMSWs), and backward volume magnetostatic spin waves (BVMSWs), with dispersion relations that differ markedly from each other [46]. This work will consider the configuration of the structure and external magnetic field by which it is possible to excite MSSWs or BVMSWs. The condition giving rise to the excitation and propagation of MSSWs within the plane of the magnetic film relates to the transverse magnetization of the waveguide structure, and the spin-wave signal propagating in the direction perpendicular to the applied magnetic field. This spin-wave type is characterized by a positive group velocity $df/dk > 0$ where k is the wave number. Conversely, BVMSWs propagate collinearly with the applied magnetic field with a negative dispersion slope and therefore negative group velocity, $df/dk < 0$ [46]. BVMSWs are excited when the magnetization of the waveguide structure is directed along the long axis, with the spin-wave propagation being collinear to the direction of magnetization. It should be understood that in most practical experimental systems, the thickness of the film is much less than the wavelength of the SW, and therefore the distribution of the wave amplitude over the thickness of the film is approximately uniform.

A uniform external magnetic field $\mathbf{H}_0$ is applied parallel to the x axis throughout all measurements and calculations. Hence, SWs propagating in section A are BVM-SWs, and those propagating in sections B and C are MSSWs [47]. The input SW signal in the area of the microstrip antenna is created by applying, along the z axis, a cw magnetic field $b_0(t) = b_0\sin(2\pi ft)$ with frequency f. The simulated spatially resolved arrays of data for the dynamic magnetization components $m_{x,y,z}$ are used to construct two-dimensional maps of the SW intensity distribution.

To calculate the spectral characteristics of spin waves propagating across the waveguides, the regions of input and output antennas are defined for each structure as depicted with red regions in Fig. 1. To excite spin waves, a broadband dynamic magnetic field $b_z(t) = b_0 \text{sinc}(2\pi f_c t)$ is applied with the cutoff frequency $f_c = 6$ GHz and amplitude $b_0 = 10$ mOe. The dynamic magnetization is recorded within the output antenna region with a time step of 75 fs for a total duration of 300 ns. The spectral power density of the output signal $P_{\text{out}}(f) = 20\log_{10}|\theta(m_\perp)|$ is constructed from the time series obtained in these sections using the Fourier transform where θ is the Fourier transform operator and $m_\perp$ is the out-of-plane component of dynamic magnetization.

To calculate the effective dispersion characteristics, the 2D Fourier transform technique is used. Spin waves are excited by the same broadband dynamic magnetic described in the preceding section. The antenna width is 50 μm. With such dimensions, it can be assumed that the alternating magnetic field of the source has a uniform distribution over the YIG film thickness. Along the center of the waveguide section, the time-varying behavior of the magnetization $m_\perp(i) = \int_V m_\perp(x,y,z,t)dV$ is recorded, where V is the volume of the region sections, the discretized time step $\Delta(t) = 75$ ns and duration $T = 600$ ns. Using the two-dimensional Fourier transform, one can extract a two-dimensional map of the distribution of the quantity

$$\mathbf{D}(k,f) = \frac{1}{N}\sum_{i=1}^{N}\theta_2[m_\perp(x,y,z,t)]|^2, \quad (2)$$

where k is the wave number, θ_2 is the 2D Fourier transform operator, i is the cell number, and $N = 256$ is the number of cells along the central section of the waveguide. The map $D(k,f)$ is the squared modulus of the magnetization amplitude and allows one to reconstruct the effective dispersion characteristics for spin-wave modes in waveguides. In the (f,k) plane, it is also possible to identify local maxima of the quantity $D(k,f)$, physically corresponding to nth-order width modes [48] with transverse wave numbers $\kappa = n\pi/w$.

B. Experimental methods

Brillouin light-scattering (BLS) spectroscopy of magnetic materials is used to reveal the spin-wave propagation along the in-plane magnonic bends with the different designs $W_{1,2,3}$. The method is based on the effect of inelastic light scattering from coherently excited magnons [49]. Light with a wavelength of 532 nm, generated by a single-frequency laser (Spectra Physics Excelsior EXLSR-532-200-CDRH), is focused to a spot with a diameter of 25 μm and power of 1 mW on the surface of the structures under study. The microwave signal from a Anritsu MG3692C signal generator is delivered to the input 30-μm-wide microstrip antenna to excite SWs. The structure is magnetized with the bias magnetic field $\mu_0 H_0 = 1200$ Oe delivered by a GMW 3472-70 electromagnet and directed along the x axis to enable the excitation of BVMSWs.

An accurate positioning system is used to obtain maps of the spatial distribution of dynamic magnetization via the BLS technique. The experiment is carried out in a quasi-backscattering configuration, with the intensity of the optical reflected signal being proportional to the square of the dynamic magnetization $I_{\text{BLS}} \sim (m_x^2 + m_y^2)$ in the optically probed region. Next, the stationary spatial distribution of I_{BLS} is obtained for different values of spin-wave input frequency. To reveal the frequency selective spin-wave channeling along the magnonic bend, the accumulation of BLS signal is collected in the same area of the virtual spin-wave detector, which is convenient for direct comparison with the results of the micromagnetic calculations.

Along with BLS, the microwave spectroscopy technique is used to obtain the matrix of complex S coefficients using a PNA-X Keysight Vector Network Analyzer (VNA). The amplitude frequency and effective dispersion characteristics are extracted via the frequency dependence of the absolute value and argument of the S_{21} coefficient in the case when the excitation and detection of the signal are achieved using a microstrip antenna.

IV. IN-PLANE MAGNONIC BEND $A_P B_P$

A. Frequency bandwidth estimation and influence of geometrical variation and bias magnetic field

In an unbounded film, BVMSWs and MSSWs exist in different frequency ranges that are separated by the frequency of ferromagnetic resonance of the YIG film $f_0 = \gamma \sqrt{H_{\text{int}}(H_{\text{int}} + 4\pi M_s)}$ [50]. The broken translational symmetry in a transversely-bounded waveguide leads to a change in the internal magnetic fields, making it possible to observe the effects of transformation of SW types in an irregular region of the waveguide system. The propagation of a spin-wave signal across the orthogonal junctions of the in-plane $A_P B_P$ occurs through a frequency shift of the dispersion branches of the BVMSW and MSSW, and

due in particular to their overlap, which characterize multiple width modes in such a geometry [50]. The calculation of the SW dispersion using micromagnetic simulations reveals the frequency range of co-existence of BVMSWs and MSSWs. On the resulting map of dispersion characteristics [Fig. 2(a)] for 500-μm-wide 10-μm-thick YIG stripes, the curves F_n and G_n ($n = 1, 2, 3$) indicate the SW width modes propagating across the A_P and B_P sections along the x axis and y axis, respectively. Here, the indices n denote the number of antinodal points characteristic of the confined SW's phase across the magnonic stripe [49,51]. The overlapping region of frequency Δf is indicated in Fig. 2(a), where the first width modes ($n = 1$) of BVMSW (F_1) and MSSW (G_1) coexist.

It should be noted that the variation of the stripes' width and thickness, along with the variation of the strength of the bias magnetic field, can tune the frequency bandwidth Δf of the magnonic interconnection.

First, we analyze the variation of $\Delta f(w, t)$ as a function of the in-plane YIG stripe's thickness (t) and width (w). Two factors affecting the value of Δf must be taken into account: (i) the internal magnetic field variation as a result of shape anisotropy [50,52], and (ii) the shift of the lower and upper cut-off frequency for MSSW and BVMSW types as a consequence of the dispersion transformation for spin waves propagating along the confined magnonic waveguide [48]. The first factor, namely the influence of the spatially varying magnitude of the internal magnetic field on the value of $\Delta f(w, t)$, can be estimated using the nonuniform profile of H_{int} inside each of the waveguides for the case of tangential magnetization [53]. Using this approach, we have estimated the bandwidth as a function of t and w. In Fig. 2(b) the value of the function $\Delta f(w, t)$ is color coded for a range of thicknesses (2.5 < t < 10 μm) and widths (250 < w < 1000 μm). It is evident that as the stripes' width decreases and thickness increases, the frequency bandwidth increases.

Factor (ii) can be analytically taken into account using the dispersion characteristics from Ref. [48] and Ref. [54]. This gives the redshift of the cut-off frequency for MSSWs along with the blueshift of the cut-off frequency for BVMSWs. Thus, factor (ii) yields a nonzero value for Δf even without taking into account factor (i). The results of micromagnetic modeling and the analytical estimation clearly give good agreement for the considered YIG film [see Fig. 2(c)], with an increase in the thickness and a decrease in the width of the waveguide structure leading to an increase in the area of coexistence of BVMSWs and MSSWs in the frequency band Δf.

Next, we analyze the influence of the bias magnetic field strength on the value of Δf_0. Note that Δf_0 is defined for both the MSSWs and BVMSWs as the difference in f_0 that arises as a result of the confinement of the continuous magnetic film. Figure 2(d) shows the dependencies of Δf_0 on $\mathbf{H}_0$ in waveguides of varying width, with the
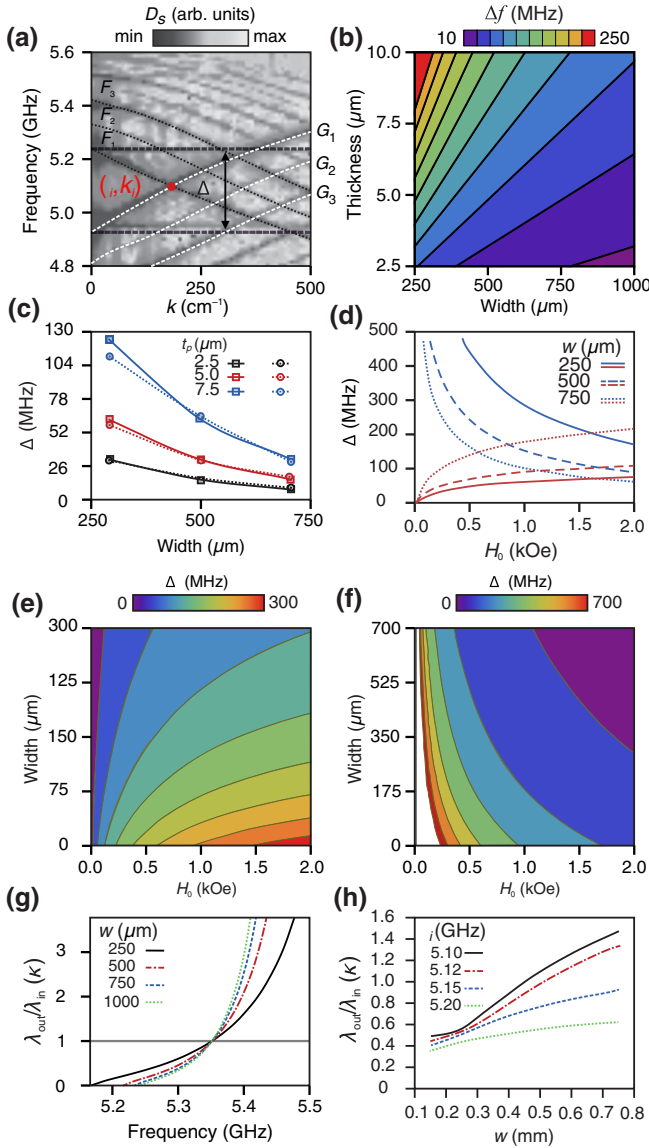
FIG. 2.   Numerical characterization of the in-plane magnonic bend with a right-angled junction. (a) Calculated map of SW dispersion characteristics across the A_P and B_P waveguide sections for 500-μm-wide YIG stripes of thickness 10 μm. (b) Color-coded map of the function $\Delta f(w, t)$ for a range of stripe thicknesses and widths as indicated. (c) Dependence of Δf on the stripe's width w and thickness t_P obtained from the micromagnetic modeling (solid curve) and analytical calculations (dotted curves). (d) Dependence of Δf_0 on $\mathbf{H}_0$ in waveguides with a width as indicated for BVMSWs (blue) and MSSWs (red), respectively. (e),(f) Color-coded map of the function $\Delta f(H_{0,w})$ for BVMSWs and MSSWs respectively. (g) Conversion factor $\kappa = \lambda_{\text{out}}/\lambda_{\text{in}}$ as a function of the frequency f with a waveguide width as indicated. (h) Conversion factor $\kappa = \lambda_{\text{out}}/\lambda_{\text{in}}$ as a function of the width of the YIG stripes w at the frequency as indicated.

blue and red curves representing BVMSWs and MSSWs, respectively. At the same time, Figs. 2(e) and 2(f) show the color-coded functions $\Delta f_0(H_0, w)$ for BVMSWs and

MSSWs, respectively. These results show that increasing H_0 results in Δf_0 increasing for MSSWs and decreasing for BVMSWs.

B. Wavelength conversion

The broken translational symmetry by the in-plane junction of magnonic stripes permits spin-wave wavelength conversion to occur, with the conservation of the SW's frequency. This can be understood from the analysis of the SW dispersion [Fig. 2(a)]. In a special case, the BVMSW at the frequency $f_i = 5.1$ GHz excited in A_P with the wave number $k_i = 200$ cm^{-1} is converted to a MSSW in section B_P with the same wave number, as depicted in Fig. 2(a) where the intersection of dispersion characteristics of both type of spin waves is highlighted. In contrast, the longer wavelength of the BVMSW at other frequencies leads to the conversion to a MSSW of shorter wavelength in B_P. The conversion factor $\kappa = \lambda_{\text{out}}/\lambda_{\text{in}}$ in the in-plane waveguide junction as a function of the frequency f is shown in Fig. 2(g). Here, λ_{in} is the SW wavelength in A_P while λ_{out} corresponds to the wavelength in the section B_P. Increasing the width of both stripes leads to an increase of the slope of $\kappa(f)$ after the point $f = f_i$ where $\kappa = 1$. As a result, κ varies more strongly for the case of wider magnonic stripes.

In the in-plane topology of magnonic waveguides, varying the thickness of sections A_P and B_P is quite challenging whereas the stripe width can be easily modified with no additional fabrication steps. Changing the width w_2 of section B_P in the case of BVMSW excitation in A_P allows one to obtain a different value of κ. Figure 2(h) reveals how the variation of w_2 influences κ for the frequency $f_i = 5.1$ GHz and the frequencies nearby. In particular, when $f > f_i$, the gradient of $\kappa(w_2)$ is larger compared to the case when $f < f_i$. This degree of freedom provides an additional opportunity for enhancing the wavelength conversion via the in-plane magnonic bend.

C. Imaging of spin-wave propagation with BLS and micromagnetic calculations

To experimentally assess both the bandwidth of the in-plane bend and spin-wave propagation across the fabricated structure, we use microwave spectroscopy and BLS. We explain our results using micromagnetic simulations.

1. BLS and micromagnetic data

The simplicity of fabricating in-plane 2D bends of magnonic waveguides using chemical- or ion beam etching or laser ablation allows us to consider different types of waveguide junctions. Using BLS microscopy, we track the propagation of spin waves across $A_P B_P$ structures with different types of joints [curved bend (W_1), right-angled corner (W_2), and a diagonal connection at 45° (W_3)]. Spatial maps of the intensity distribution I_{BLS} for the values of the
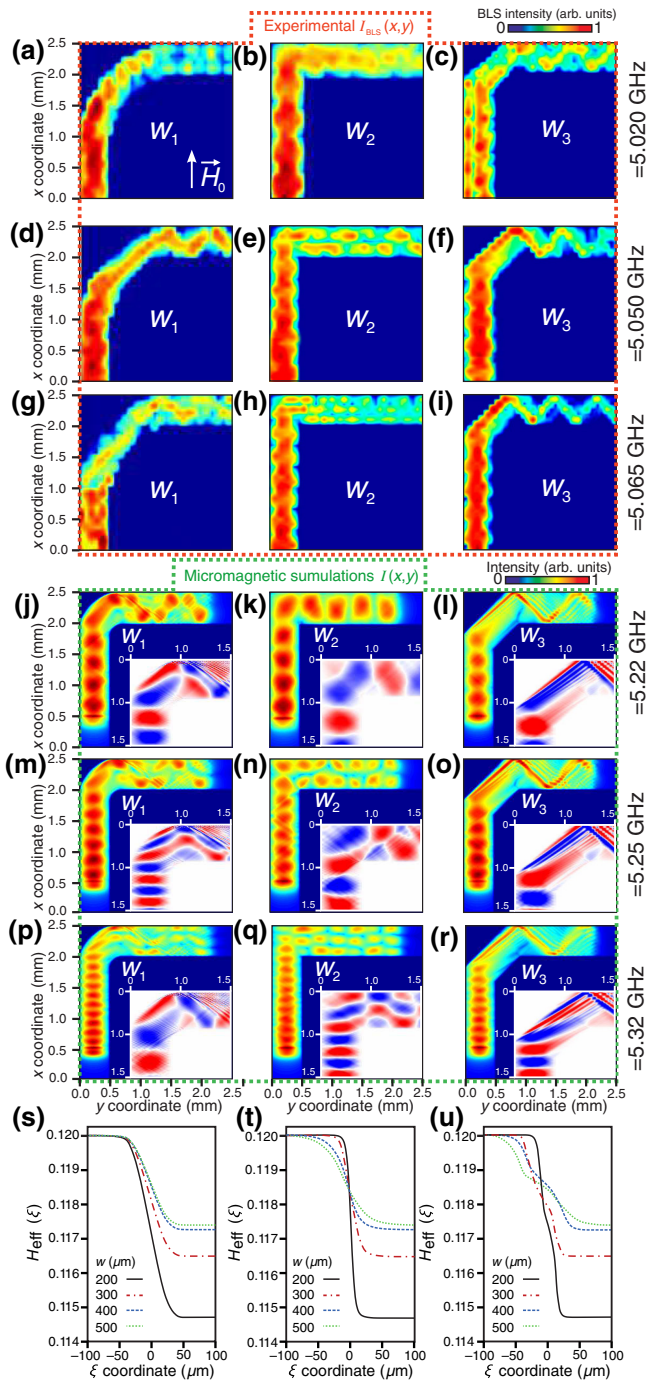
FIG. 3. (a)–(i) Spatial distribution of the BLS signal at 5.020, 5.050, and 5.065 GHz. (j)–(r) Spatial distribution of intensity of dynamic magnetization $I(x,y)$ at frequencies 5.22, 5.25, and 5.32 GHz. (s)–(u) Dependency of effective magnetic field $H_{eff}(\xi)$ for bends W_1, W_2, and W_3 with different stripe widths as indicated.

input signal frequency $f_1 = 5.020$ GHz, $f_2 = 5.050$ GHz, and $f_3 = 5.065$ GHz are presented in Figs. 3(a)–3(i). The structures are always subject to an external magnetic field $\mathbf{H}_0 = 1200$ Oe directed along the x axis for effective

excitation of the BVMSW in the input section A_P [50,55]. The input signal power is $P_0 = -10$ dBm, ensuring that the SWs are always in the linear regime of excitation and propagation. Spatial scanning is carried out in an area of size 2.5×2.5 μm^2.

To understand the process of spin-wave transmission we use micromagnetic calculations alongside the BLS measurements to map the spin-wave intensity $I_{BLS}(x,y) = (m_x^2 + m_z^2)$ across structures $W_{1,2,3}$ with the same parameters as in the experiment. The results of the numerical simulations are presented in Figs. 3(j)–3(r). It should be noted that the overall features of the measured SW intensity maps are well reproduced by the calculations. By then performing a mode decomposition [49,56] of the spatial spin-wave intensity distribution, one can observe that the interference of the width modes produces a characteristic "snakelike" or "zig-zag" structure of SW-intensity inside the section B_P. Across the waveguide with the rounded connection W_1 (first column of images in Fig. 3), the BVMSW propagating along the section A_P is transformed [55,57] in the bending region to a MSSW propagating along section B_P. Strictly speaking, one cannot refer to these waves as MSSWs and BVMSWs due to these only being defined for a continuous magnetic film [48,50–52,58], but for convenience we refer to the types of the waves as MSSW and BVMSW as having the different sign of the gradient of dispersion. Changing the frequency of the input signal allows one to control the mode composition of the spin-wave signal in the B_P section. For the case of the waveguide junction consisting of a right-angled bend (second column of images in Fig. 3), the mode composition of the MSSW with increasing frequency propagating in the B_P section changes [48,49,51,59–61]. At the frequency $f = 5.020$ GHz, for example, the BVMSW excited in the A_P section propagates through the bend and converts to a MSSW while maintaining its modal composition. By increasing the frequency to $f = 5.050$ GHz, it is possible to instead obtain a two-mode regime of propagation mode of the MSSW [60,61] [see Fig. 3(e)]. A further increase in the frequency to $f = 5.065$ GHz makes it possible to excite the third mode of the MSSW in the B_P section [see Fig. 3(h)]. Thus, it is clear that the interconnection method could be inherently used to select the spin-wave width mode in the output section of the L-shaped structure, without the need to utilize the effects of intermodal dipolar spin-wave coupling described in Ref. [62]. The inset panels of Figs. 3(j)–3(r) show the distribution of the m_z component of magnetization in the region of broken translational symmetry.

2. Enhancement of spin-wave transmission across the bend

The design of magnonic bends in the form of 45° connections (third column of images in Fig. 3) provides

for the superposition of symmetric and antisymmetric modes in the B_P section, manifesting as a "snakelike" or "zig-zag" pattern of spin-wave intensity inside B_P. As already demonstrated in Fig. 2(a), the spin-wave spectra inside B_P consists of $G_{1,2,3}$ modes. The characteristic "snakelike" pattern is formed mainly from the contribution and interference of co-propagating G_1 and G_2 modes [43,48,49,51,56].

Here we should note that the efficiency of spin-wave propagation across the bend is mainly governed by the two factors as already elucidated: (i) nonuniform profile of internal magnetic field in the bending region [35]; (ii) the broken translational symmetry, which leads to the formation of SW width modes with finite transverse wave numbers. The latter, in particular, defines the conditions of an excitation of high-order modes of spin waves in the B_P section.

The first factor was introduced in Ref. [35] for rounded magnonic bend when the orientation of the in-plane bias magnetic field was varied. Here, we analyze the variation of the internal magnetic field profile $H_{\text{eff}}(\xi)$ across the curvilinear ξ coordinate within different junctions $W_{1,2,3}$. The profiles $H_{\text{eff}}(\xi)$ [see Figs. 3(s)–3(u)] are obtained from the solution of the static problem, where the magnetization is relaxed according to the micromagnetic solution of Eq. (1) with the applied static magnetic field H_0 directed along the x axis. Figures 3(s)–3(u) show $H_{\text{eff}}(\xi)$ for W_1, W_2, and W_3 bends of different waveguide widths in the range $200 < w < 500\,\mu\text{m}$. The internal magnetic field $H_{\text{eff}}(\xi)$ in the A_P section practically coincides in magnitude with the external bias field H_0. This correspondence emerges from the fact that an external magnetic field is applied along the length of a part of the A_P section and, as a consequence, the static demagnetizing field is zero [63]. The reduction of $H_{\text{eff}}(\xi)$ for $\xi > 50\,\mu\text{m}$ in section B_P is associated with the presence of a large demagnetizing field H_{demag}, since the external magnetic field is applied along the short axis of B_P. It is clear that the step size in $H_{\text{eff}}(\xi)$ across the junction increases with reducing waveguide width due to the more pronounced effect of shape anisotropy for the narrower magnetic stripe [50,59]. Quantitative comparison of Figs. 3(s)–3(u) reveals that the rounded bend features the longest path for the propagating spin wave in the almost linearly decreasing profile of $H_{\text{eff}}(\xi)$ across the bending region. Figure 3(s) shows a smooth drop of the internal field $H_{\text{eff}}(\xi)$ across the rounded connection in contrast to the sharper change in $H_{\text{eff}}(\xi)$ associated with the right-angled junction [Fig. 3(t)]. In the case of the 45° connection, similar smooth variation of $H_{\text{eff}}(\xi)$ is observed albeit with an interruption corresponding to the waveguide segment connecting the magnetic strips A_P and B_P.

The second interpretation of the variation of the spin-wave transmission efficiency can be associated with the propagation of a SW beam that undergoes multiple reflections from the geometrical edges of the waveguide, according to the (generally anisotropic) laws of spin-wave optics across the magnonic bend in the nonuniform profile of internal magnetic film [35,64,65]. This is accompanied with the propagation of the causticlike beam inside the 45° connection, which is close to the cut-off angle of magnetostatic spin-wave propagation in the tangentially magnetized YIG film [31,66,67]. Figure 4(a) schematically shows the isofrequency curve for SWs propagating in the in-plane magnetized ferromagnetic film of YIG [50,67]. The orange curve in Fig. 4(a) shows the spectra of transverse wave numbers k_y in the case of spin-wave diffraction from the end of the first waveguide section [55,65–70]. This sketch demonstrates that the spin-wave group velocity points along the same direction as the junction section of W_2 for wave numbers satisfying the condition $k_y < 50\,\text{cm}^{-1}$ [55,65,66].

To elucidate the influence of the aforementioned factors (i) and (ii) on the spin-wave transmission across the bend, we next concentrate on the transmission spectra obtained with microwave measurements, BLS microscopy, and micromagnetic techniques. Figure 4(b) shows the results of microwave measurement of the absolute value of frequency transmission coefficient S_{21} of the signal in the output sections B_P for the different bends $W_{1,2,3}$. Here, we use the microwave microstrip line to excite and detect spin-wave precession in the area of the short-circuited microstrip transducers [see inset in Fig. 4(b)]. It can be seen that the BVMSW propagating along the input section is transformed into a MSSW, while the signal power frequency spectra at the output in the structures W_1 and W_2 is almost equal. In the magnonic bend comprised of two sections interconnected at an angle of 45°, the signal transmission is higher. The BLS method is also appropriate for measuring the frequency dependence of the spin-wave intensity at the output region inside B_P [58,71]. To plot the frequency dependencies for each design of bend, we integrate the BLS signal collected within the area of the output transducer, which was previously used for the VNA measurements [as depicted with the light cone shown in the inset of Fig. 4(c)]. Analysis of the BLS data and micromagnetic simulation, presented in Figs. 4(c) and 4(d), respectively, also reveals the better transmission for the diagonal design of the bend (W_3). The image shown in Fig. 4(a) can qualitatively explain the enhanced spin-wave transmission across the diagonal bend, since the direction of the SW group velocities in this configuration almost universally coincides with the angle of the section connecting the stripes A_P and B_P [72]. The variation of the SW wavelength after turning a corner can also affect the propagation length, firstly due to the different group velocities of the SW wave in sections A_P and B_P and secondly due to the propagation length decreasing with the wavelength reduction, since the spin-wave propagation length is defined by the intrinsic damping of YIG along with the wavelength
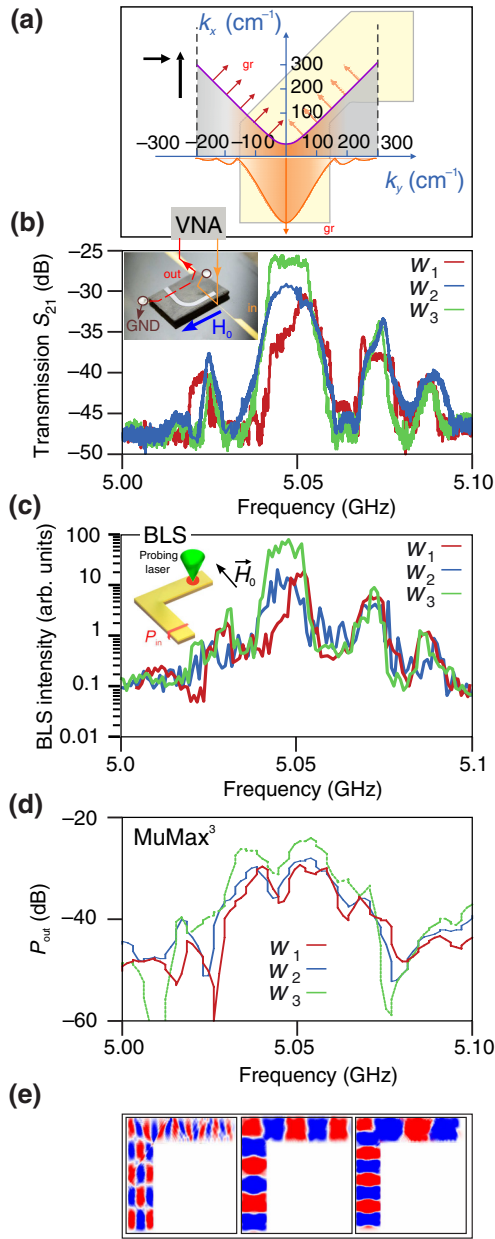
FIG. 4. (a) Schematic visualization of isofrequency curves characteristic of SWs propagating across the diagonal junction. The magnetic field H_0 is directed along the x axis. (b) Microwave measurement of the absolute value of frequency transmission coefficient S_{21} of the signal in the output sections B_P by VNA for bends with different types of connections $W_{1,2,3}$. (c) Intensity transmission measured by BLS in the B_P section for bends $W_{1,2,3}$. (d) Frequency transmission coefficient of the output signal power (obtained by numerical simulations). (e) Wavelength conversion in $A_P B_P$ structure for the cases of $f < f_i, f = f_i$ and $f > f_i$.

(damping per unit of wavelength). The situation with the variation of dispersion slope is not addressed here since this factor becomes significant only when the YIG waveguide's width approaches $100\,\mu$m for a stripe thickness of $10\,\mu$m. The second situation with the wavelength variation

after the SW turns the corner manifests in the distinct lobes in the frequency dependence of S_{21}: the SW signal undergoes wavelength transformation according to the width-mode dispersion spectra shown in Fig. 2(a). This is clearly confirmed by the numerical simulations shown in Fig. 4(e), where three situations are considered: conversion to the longer wavelength ($f < f_i$), conservation of the wavelength ($f = f_i$), and conversion to the shorter wavelength ($f > f_i$).

Thus the geometrical design of the bend in the form of different junctions and variation of the width and thickness of the bends' sections opens a way towards fabricating a magnonic interconnect unit with predefined frequency bandwidth and wavelength conversion facility.

V. OUT-OF-PLANE MAGNONIC BEND $B_V C_V$

A. Variation of waveguide thickness

The transmission of a SW signal in the out-of-plane direction represents one of the pathways towards increasing the number of computational elements in MNs. The use of orthogonally connected magnetic strips provides a straightforward means to fabricate out-of-plane waveguides within a three-dimensional structure, e.g., meander-shaped waveguide [26–29]. The study of spin-wave transport in periodic YIG meander structures, in the Bragg and Laue geometries, demonstrate the possibility of using the meander structure as a system of coupled resonators that are formed by flat segments of the three-dimensional structure [29]. In that work, however, the propagation of SWs through a vertical section was not explored. To therefore elucidate the mechanism of signal transmission across the $B_V C_V$ structure [Fig. 1(c)] with broken translational symmetry across the y-z plane, we employ micromagnetic calculations. The structure is always subject to an external magnetic field $H_0 = 1200$ Oe directed along the x axis for the effective excitation of the MSSW in the B_V section. Since the concept of magnonic logic [6] is based on the use of spin-wave interference effects, both the amplitude and phase of the SW in the output section of the structure are valuable [11,12]. At the same time, the peculiar SW-related features of the 3D magnonic meander structure are known to emerge from a nonequal thickness of the vertical and horizontal segments [26,27].

Next we consider the spin-wave propagation across the $B_V C_V$ bend with a $t_{V1} = 10$-μm-thick in-plane B_V section with varying thickness of the out-of-plane waveguide t_{V2} (in the range $2.5 < t_{V2} < 10\,\mu$m). For this purpose, the cw signal $b_0(t) = b_0\sin(2\pi ft)$, where $b_0 = 0.1$ Oe with a predefined frequency $f = 5.1$ GHz, is applied along the z axis in the region highlighted red in Fig. 1(c). The resulting dynamic magnetization is recorded for a total duration of 300 ns across the entire $B_V C_V$ structure. The spatial distribution of the dynamic magnetization intensity $I(x,y)$ in B_V and $I(z,y)$ in C_V, and the distribution
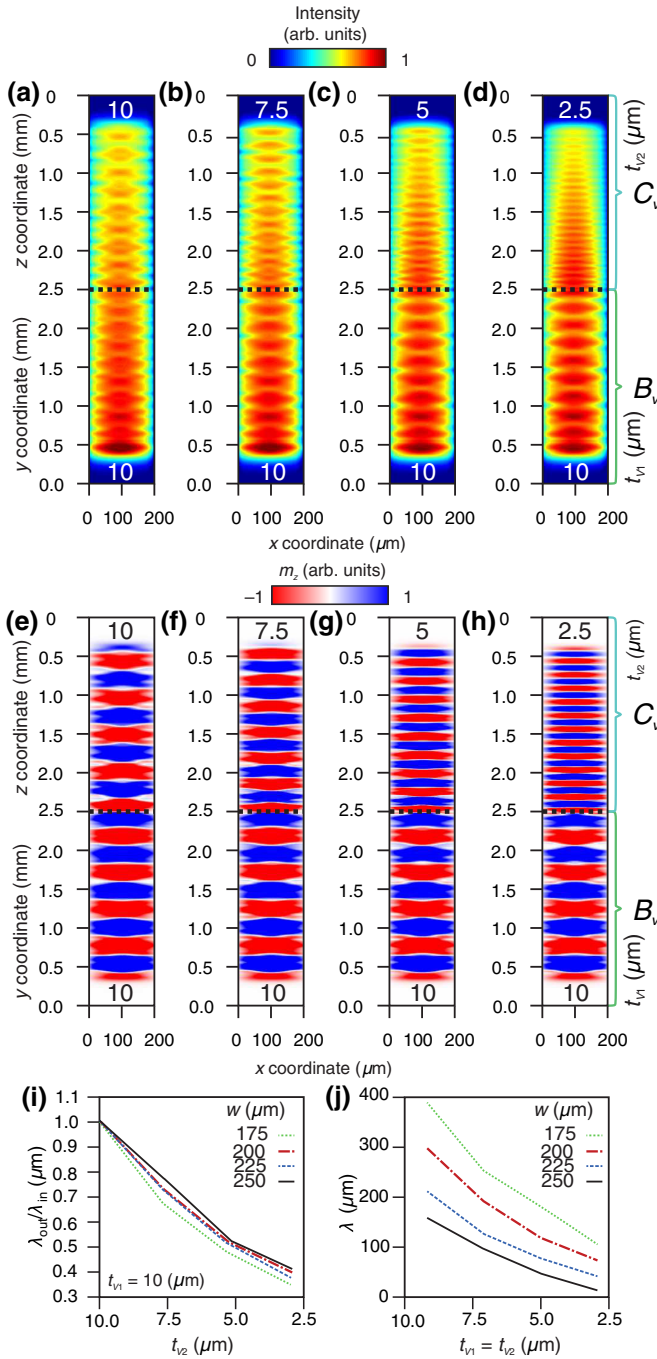
FIG. 5. (a)–(d) Spatial distribution of $I(x,y)$ with width $w = 250\,\mu m$. (e)–(h) Spatial distribution of the $|m_x|^2$ component of dynamic magnetization at a frequency of 5.1 GHz at $w = 250\,\mu m$. (i) Dependence of the wavelength in the C_V section on the thickness t_{v2} of the out-of-plane waveguide with varying width as indicated. (j) Dependence of the wavelength in the C_V section on the thickness $t_{V1} = t_{V2}$ with varying width as indicated. All data shown is obtained at 5.1 GHz and $H_0 = 1200$ Oe.

of the dynamic component of the magnetization $|m_z|$, are shown in Figs. 5(a)–5(h), respectively. It is apparent that the wavelength of the SW propagating along C_V is shorter

compared to that in B_V. Here we must note that the type of magnetostatic spin wave is conserved across $B_V C_V$ since the SW's wavevector is persistently orthogonal to the static magnetization. Varying the thickness t_{V2} of section C_V, however, leads to significant changes of the contribution of volume magnetic charges on the dispersion of the propagating MSSW [50,52]. At the same time, the fact that the demagnetizing field H_{demag} decreases in strength for thinner waveguides leads to an enhancement of H_{eff} across C_V when t_{V2} decreases, making it possible to excite SWs with shorter wavelengths at the fixed frequency. This is confirmed by the results of micromagnetic calculations shown in Fig. 5(i), which also shows that—for narrower stripes—the conversion factor $\kappa = \lambda_{out}/\lambda_{in}$ is smaller for higher values of t_{V2}. Furthermore, if the width of both sections B_V and C_V is increased simultaneously when $t_{V1} = t_{V2}$, the SW wavelength decreases, while simultaneously increasing the thickness $t_{V1} = t_{V2}$ leads to an increase in the SW wavelength [Fig. 5(j)].

It should be noted that a step in thickness across a single YIG waveguide leads to the formation of a region with inhomogeneous internal magnetic field profile, which serves as the source region for short dipolar-exchange SW generation [73]. The out-of-plane $B_V C_V$ waveguide structure, with nonequal thickness of each section, can also be used to generate short-wavelength SWs since it can be considered as an unfolding of the waveguide presented in Ref. [73].

B. Experimental proof of concept of the out-of-plane junction of two YIG stripes

In comparison with that of the in-plane junction, the frequency bandwidth in the $B_V C_V$ structure is expected to be larger since the SW preserves its dispersion type in both sections. Here, we note that for a single waveguide of length $l_2 + l_3$, the bandwidth of the excited SW can be limited either by the magnetostatic wave dispersion or by the antenna width. The former factor gives $\Delta f = \gamma[H_0 + 2\pi M_s - \sqrt{H_0(H_0 + 4\pi M_s)}] = 542$ MHz for $H_0 = 1200$ Oe whereas the latter gives $\Delta f = 0.5$ GHz for an antenna width of 30 µm. Figure 6(a) shows the results of micromagnetic calculations of the spectral power density P_{out} directly before the junction in section B_V (solid black curve) and in the output section of C_V (red dotted curve). The bandwidth of signal transmission is identified to be $\Delta f = f_2 - f_1 = 0.63$ GHz.

Using the phase shift evaluated by the micromagnetic calculations, the effective wave numbers are estimated in the excitation frequency range $[f_1, f_2]$ using the relationship $k_{eff} = (\psi(f) - \psi_0(f))/l_s$ where $\psi(f) = \int_0^{l_s} k(o)do, (o = y, z)$ is the SW's phase shift across the length l_s between the input and output of each section, $s = 2$ for B_V and $s = 3$ for C_V and $\phi_0(f)$ is the initial phase of the SW source. Figure 6(b) shows the calculated SW dispersion with the
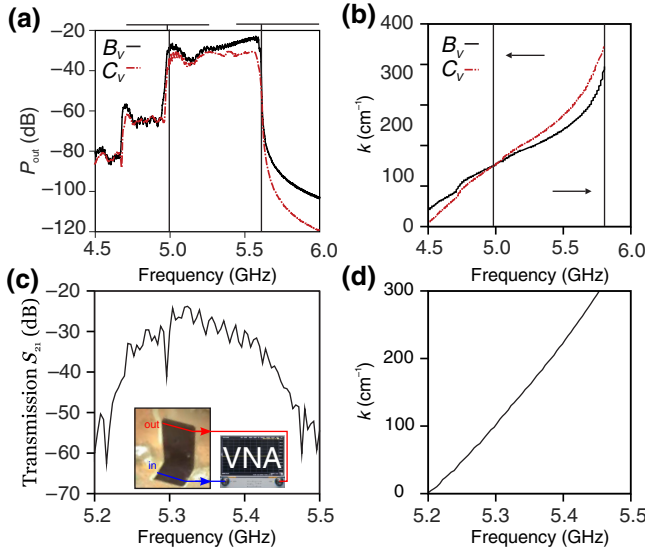
FIG. 6.   (a) Numerical results of micromagnetic calculations of the spectral power density P_{out} and (b) dispersion at the output of the B_V section (solid black curve) and the C_V structure (red dotted curve). (c) Experimentally measured SW transmission S_{21} and (d) phase-frequency response in the vertical structure obtained using VNA measurements at the output of the $B_V C_V$ structure.

points of coincidence highlighted where $f(k_{eff})$ overlap for the SW propagating across the B_V and C_V sections. This indicates that the SW propagates across the out-of-plane junction without transformation of the magnetostatic wave type. In light of this, the variation of the design of the magnonic out-of-plane junction bend is clearly not crucial, in contrast to the sensitivity associated with the in-plane junction. The same situation occurs for FVMSWs propagating along the in-plane junction $A_P B_P$ [33], where the SW preserves its type throughout the entire structure.

To perform an experimental study of the spin-wave transport across the out-of-plane junction, the structure is fabricated by orthogonally connecting two short-circuited microstrip lines with the same ground screening electrode [see inset in Fig. 6(c)]. The magnonic waveguides had a width and thickness of 500 and 10 μm, respectively. S parameters are measured by microwave spectroscopy using a VNA connected to the microstrip line in the same fashion as with the in-plane junction. Figure 6(c) shows the signal detected using the microstrip transducer positioned at the output of section C_V while the MSSW is excited in the input section of B_V. The bandwidth estimated from our experimental measurement is on the order of 250 MHz, which is smaller than Δf obtained from the micromagnetic calculations. We attribute this discrepancy to a mechanical gap existing at the junction of two YIG waveguides. We emphasize, however, that this experimental result serves as a proof of concept of spin-wave transport in the orthogonal junction of two sections. The more physically real and applicable situation arises in,

e.g., meander-shaped waveguides either in the micromagnetic approach [74] or in BLS and/or microwave studies [26,27,29]. The dip in the frequency dependence of transmission presented in Fig. 6(c) can also be associated with the integer number of half-wavelengths between the input antenna and the junction area of B_V and C_V. The dip at 5.3 GHz, in particular, is caused by the presence of an air-gap, which inescapably arises from the mechanical connection between the B_V and C_V sections. The spin-wave dispersion reconstructed from the phase-frequency characteristics corresponds to the MSSW dispersion, further proving that the spin-wave type is conserved as the SW propagates across the out-of-plane junction [see Fig. 6(d)].

Thus, the out-of-plane connection of two YIG stripes can also be used to design predefined characteristics of signal transmission with the change of the group-velocity direction. Our results show that the amplitude and phase of the SW can be easily estimated by exploiting the fact that the SW-type is preserved across such a structure.

VI. THREE-DIMENSIONAL JUNCTION *ABC*

Here we focus on the structure *ABC* depicted in Fig. 1(a). During its transport across *ABC*, the spin wave is subject to twofold symmetry breaking. The two junctions in the lateral (*x*-*y* plane) and vertical (*z*-*y* plane) sections can be used both to connect functional magnonic elements and as frequency-filtering and wavelength-conversion units themselves.

Experimentally, we study the three-dimensional magnonic junction—composed of three YIG stripes shown on Fig. 7(a)—made by mechanically connecting two YIG waveguides. The waveguide sections A and B are made in the form of a single L-shaped waveguide with width $w = 500$ μm and length $w = 2.5$ mm, formed using laser ablation of double-sided YIG/GGG/YIG film. A vertical section C of the same width is mechanically attached to the end of section B. The experimental transmission coefficient S_{21} [black solid curve in Fig. 7(b)], measured with an external magnetic field $H_0 = 600$ Oe, reveals bandwidths up to
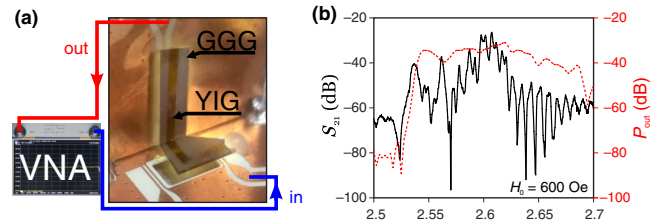

FIG. 7.   (a) Experimental setup three-dimensional *ABC* magnonic junction. The bias magnetic field with strength $H_0 = 1200$ Oe is directed along the long axis of section A throughout. (b) Experimentally measured SW transmission S_{21} (black solid curve). Numerical results of micromagnetic calculations of the spectral power density P_{out} (red dotted curve).

100 MHz. Micromagnetic modeling with the same external magnetic field demonstrates a similar form of the transmission coefficient [red dotted curve in Fig. 7(b)] in the same frequency range. The observed dips in the experimental data are associated with the air gap at the connection with out-of-plane section. This reveals itself with the spin-wave reflection from the interconnection area, and could form a separate topic of investigation although it is beyond the scope of our work here.

Next, the spectral characteristics of the SW transport across the three-dimensional junction ABC are obtained using micromagnetic calculations. Throughout, the structure is subject to a bias magnetic field $\mathbf{H}_0 = 1200\,\mathrm{Oe}$ directed along the x axis in order to efficiently excite BMSWs along section A. The power spectral density of the output signal is extracted from the time-resolved calculations, obtained across the cross sections at the outputs of each of the A, B, C sections using the Fourier transform. The effective wave numbers are also calculated in the frequency range where BVMSW and MSSW can exist as $k_{\mathrm{eff}} = (\psi(f) - \psi_0(f))/l_s$, where $\psi(f) = \int_0^{l_s} k(o)do$, $(o = x, y, z)$ is the SW's phase shift in the corresponding section relative to the initial phase at the source.

Figure 8(a) shows the BVMSW power spectral density $P_{\mathrm{out}}(f)$ obtained at the output of section A. The bandwidth is $f_4 - f_1 = 1.424\,\mathrm{GHz}$. The high-frequency oscillations of P_{out} close to f_4 originates from there being an integer

number of half-wavelengths between the input antenna and junction area of sections A and B, similar to the case of the out-of-plane bend.

The dips at the frequencies f_2 and f_3, and the sharp drop at f_1, are associated with the antenna width used in the simulations. The frequency range above f_4 corresponds to higher-order BVMSW modes. Figure 8(b) shows that in section A, the dependence $k_{\mathrm{eff}}(f)$ corresponds to that of a BVMSW, and qualitatively coincides with the dispersion dependence for the F_1 BVMSW mode calculated for section A_P as shown earlier in Fig. 3(a).

The power spectral density for MSSWs obtained at sections B [Fig. 8(c)] and C [Fig. 8(e)] reveals the presence of a region $f_5 < f < f_4$ where the effective propagation of MSSWs and BVMSWs occurs [as depicted in red in (c) and (e) of Fig. 8]. It should be noted that the bandwidth of the signal propagation through ABC is defined mainly by the frequency range where MSSWs and BVMSWs coexist. The dependency $k_{\mathrm{eff}}(f)$ cannot be extracted at the end of B section since the dispersion in each of the sections have different gradient. At the same time, the phase shift for the signal detected at the end of the B section can be straightforwardly extracted from the simulation [see Fig. 8(d)]. Finally, the frequency dependence of the phase $f(\psi)$ has the positive slope as for MSSW modes. Note the form of $f(\psi)$ here corresponds to the sum of the phase shift across both sections A and B.
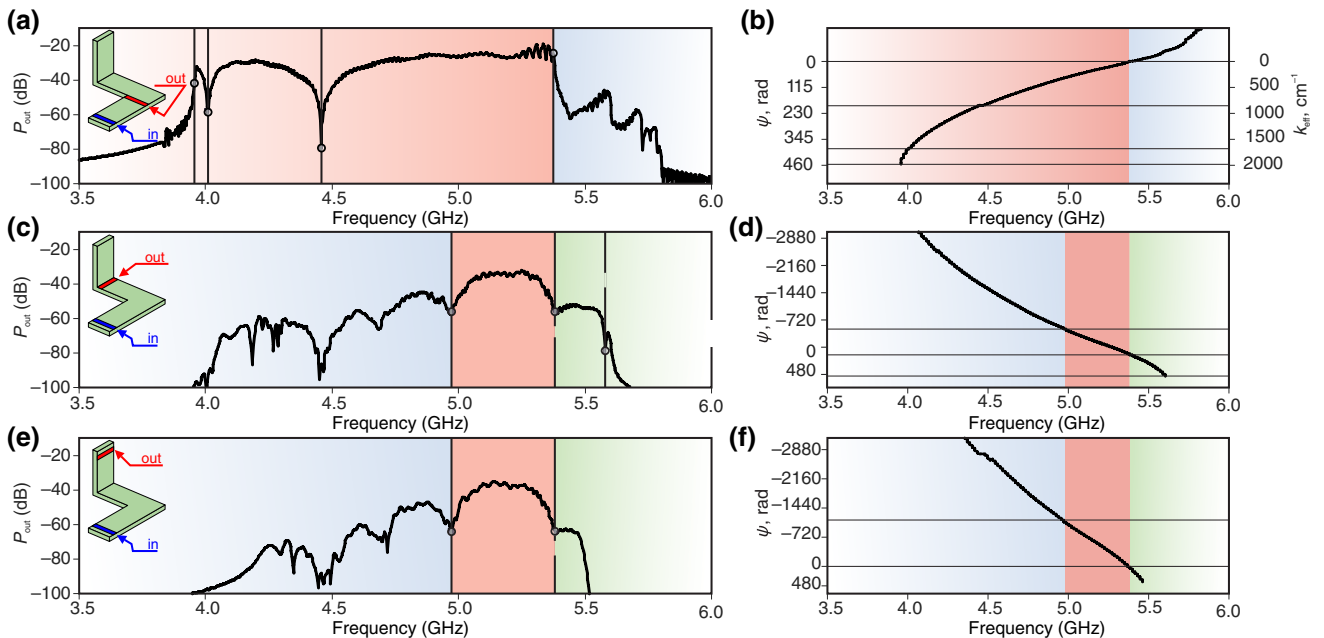

FIG. 8. Results of micromagnetic calculations of the three-dimensional magnonic junction. (a) Spectral power density $P_{\mathrm{out}}(f)$ evaluated at the region indicated in the inset, and (b) the corresponding phase $\psi(f)$. (c)–(f) The same type of result as shown in (a) and (b) obtained at different positions as indicated in the insets. Note the axis of the frequency dependence of the effective wave number $k_{\mathrm{eff}}(f)$ is inverted and is only plotted for section A where the BVMSW is excited and propagated. The bias magnetic field with strength $H_0 = 1200\,\mathrm{Oe}$ is directed along the long axis of section A throughout.

In the region below the frequency f_5, the higher MSSW width modes can be distinguished as the lobes in the spectra as in Ref. [35]. The phase-frequency dependence at the end of section C also has a positive slope as for MSSWs. Here we conclude that the design of a three-dimensional magnonic junction—based on two bends—gives rise to the possibility of frequency-selective wave propagation with the intrinsic attenuation deriving mainly from the material (for YIG, 20-dB losses for the path after section A to the end of section C). At the same time, the phase shift for this structure can be easily calculated and the predefined phase-frequency characteristics also provides the facility to construct, e.g., a Mach-Zender interferometer scheme for 3D magnonic circuitry.

VII. SPIN-WAVE PROPAGATION IN NANOSCALE YIG MAGNONIC BEND

In light of the requirements of engineering solutions to reduce the geometric dimensions of functional magnonic blocks [75,76], we must consider the transition to nanometer-sized structures with broken translational symmetry. Until recently, the transition of magnonic devices to the nanoscale region remained impossible due to limitations in the fabrication technologies, but recent studies have now shown the first steps towards the design and practical realization of nanoscale magnonic networks [9,77–82]. The fabrication of nanoscale waveguide structures, while maintaining the $\theta = w/t$ aspect ratio in the $A_P B_P$ magnonic bend, provides us with the possibility of transforming the spin-wave signal from BVMSW to MSSW type. It should be noted that the nanostructuring method renders it possible to fabricate YIG strips with a width-to-thickness ratio close to 1 [79], in contrast to the micrometer-thick YIG films with the trapezoidal shape of the waveguide edge due to the typical anisotropic chemical etching of the YIG crystal structure.

The physical phenomena of the SW turn in the nanoscale magnonic bend remains the same as for micron-sized YIG films, with the exception of three peculiar features, which should be considered for nanoscale magnonic waveguides: demagnetization, exchange interaction for short SWs, and the pinning condition for dynamic magnetization. Firstly, we consider the variation of the internal magnetic field across the waveguide with submicron width. Figure 9(a) shows the dependence of the internal magnetic field across a transversely magnetized waveguide structure on the width for an L-shaped waveguide with a thickness of $d = 50$ nm and $d = 100$ nm. The significant dependence of the internal magnetic field H_{int} on the waveguide's width allows one to explore the possibility of spin-wave transport across submicron-thick YIG waveguides with broken translational symmetry. The inset of Fig. 9(a) shows the distribution of the internal magnetic field across an L-shaped structure with the width $1 = 1$ μm and thickness
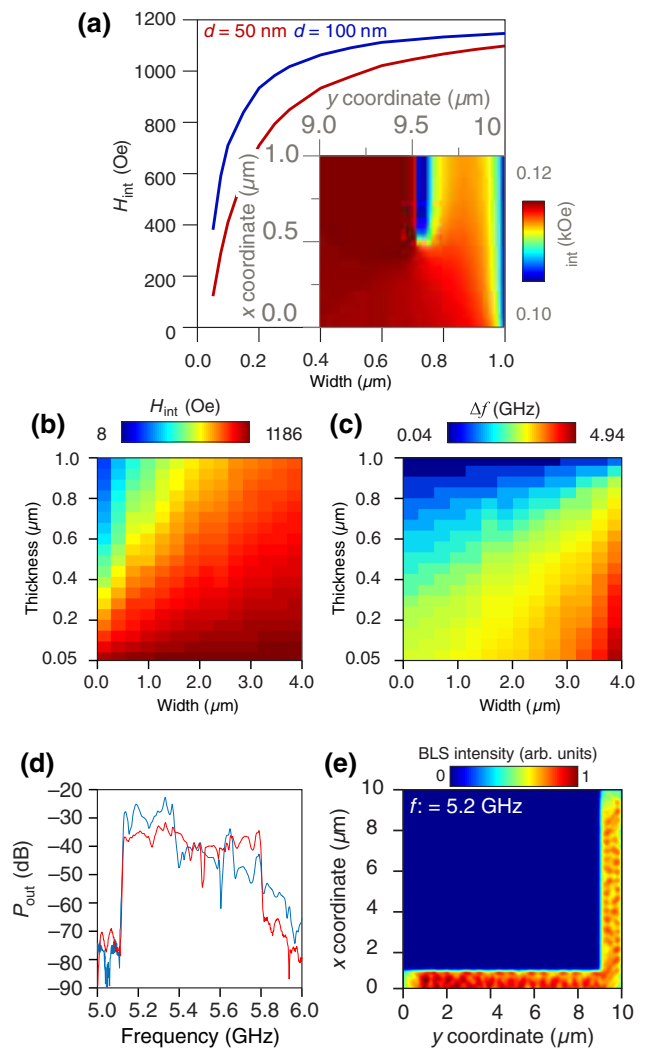

FIG. 9. (a) Dependencies of the internal magnetic field on the width of the YIG microwaveguide with the thickness $d = 50$ nm and $d = 100$ nm; (b) distribution of the value of the internal magnetic field as a function of width and thickness; (c) Δf as a function of with and thickness; (d) the spectral power density of the output signal in a YIG magnonic bend with a film thickness $t = 100$ nm; (e) the distribution of the magnetization intensity at the frequency $f = 5.2$ GHz. All data are presented for $H_0 = 1200$ Oe.

$d = 50$ nm, which reveals the reduction of H_{int} in the orthogonal section. The inset in Fig. 9(a) shows the distribution of the internal field in the region of broken translational symmetry, for a waveguide structure with a width of 500 μm and thickness of 100 nm subject to an external magnetic field $H_0 = 1200$ Oe. With the simultaneous variation of d and w, the value of H_{int} could be controlled as shown in Fig. 9(b). The larger the value of θ, the smaller the internal magnetic field becomes in the center of the waveguide. Figure 9(c) shows a map of the frequency band Δf for a submicrometer-thick YIG waveguide, which

indicates the possibility of spin-wave transport in nanometer structures with in-plane broken translational symmetry. The widest bandwidth can be achieved when minimizing θ. Figure 9(d) shows the transmission spectra of a spin-wave signal in a nanoscale planar waveguide with a film thickness $d = 100$ nm. It should be noted that the increase of the frequency inside the band Δf is accompanied with the reduction of the MSSW to BVMSW (and vice versa) transformation (see Sec. A for details). This leads to a reduction of the spectral power density close to the high-frequency edge of the band Δf. The map of the distribution of dynamic magnetization intensity at a frequency $f = 5.2$ GHz presented in Fig. 9(e) demonstrates the practical possibility of transmitting a SW signal in nanoscale waveguides with broken translational symmetry.

In Ref. [83], Wang *et al.* found that the exchange interaction becomes dominant in comparison with the dipole interaction responsible for the dipole pinning phenomenon, when the aspect ratio of width to width is close to 1:1. In this scenario, the distribution of the internal magnetic field in the structure becomes uniform. This leads to the transformation of SW modes if the width of the waveguide becomes smaller than a certain critical value [83]. Such exchange decoupling leads to a transformation of the spin-wave mode profile in nanoscopic waveguides, in contrast to the cosinelike profiles in micrometer-width waveguides, while also reducing the SW's total energy and frequency. Moreover, the exchange-dominated SWs in the MSSW and BWMSW geometry propagate with significant group velocity [50,84] and in the frequency range limited to the maximum wave-number value, which is defined experimentally by the antenna width. As the waveguide's width approaches below but increasingly closer towards a certain critical value for waveguides of nanometer thickness, the exchange interaction becomes dominant with respect to the dipolar interaction, which is responsible for the phenomenon of dipolar pinning [83,85,86]. This depins the SW modes, in turn leading to a quasiuniform profile of the spin-wave mode in nanoscopic waveguides, in contrast to the cosine-shaped profiles in micrometer-wide waveguides [47]. Consequently, the total energy and frequencies are reduced compared to the case of complete or partial pinning. The effective width of the waveguide is given by

$$w_{eff} = w[p/(p-2)], \qquad (3)$$

where $p(\theta) = 2\pi\theta/1 + 2\ln(\theta)$ [85] leads to the change of the SW's dispersion and thus the transverse wave vector of surface-localized SWs [51,58] $k_x = n\pi/w_{eff}$, and n is the number of the width mode. As shown in Ref. [83,85], the increase of w_{eff} with the decrease of θ leads to a reduction of the surface-localized SW's cut-off frequency (Fig. 4 in Ref. [85]). This results in the increase of the frequency band Δf in the magnonic nanoscopic bend.

Finally, it should be noted that strong nonuniform internal field distribution in the case of transversely magnetized waveguides leads to two modes of spin-wave propagation: fundamental modes and edge modes [87]. Edge modes are confined in narrow channels at the edges of waveguide. This phenomena could also accompany the process of spin-wave bending in L-shaped junctions, although this topic lies outside the scope of the current investigation.

VIII. APPLICATIONS OF THE MAGNONIC BEND

Existing implementations of magnon computing networks based on configurable magnon blocks have so far been demonstrated as planar devices with a single computing layer. The use of efficient blocks that enable the transmission of a SW signal in the vertical direction opens up the possibility of building a multilevel magnonic network architecture (see, for example, the sketch shown in Fig. 10). The variation of the design of the magnonic bend in both planar and vertical directions opens the possibility to use the interconnection units with functionality more tailored to the desired signal-processing task.

Next, we discuss the use of magnonic bends for mode-conversion functionality. The mode-type transformation leads to the fact that the total phase shift of the spin wave at the end of the output arm is constant. This is due to the fact that the spin waves propagating in the input and output arms have a phase shift that increases and decreases, respectively. Thus, the overall phase shifts can cancel each other, resulting in a SW pulse that retains its shape after passing through a curved waveguide (if damping is neglected). These conclusions are useful for the possible formation of bright and dark time solitons [88,89].
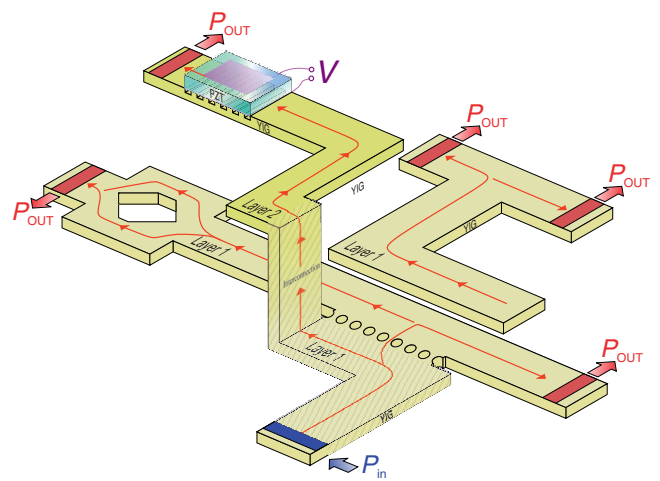

FIG. 10. Schematic structure of a multilevel magnon network consisting of configurable blocks in the form of logic devices based on magnonic crystals, interferometers, coupled waveguide, spin-wave signal splitters.

Magnonic bends have great potential as logic devices. On the basis of magnonic logic, a number of devices have already been proposed, such as logical gates [90] and three- [91,92] and four-port [93,94] devices. A key requirement for developing an integrated circuit based on magnon logic is a long propagation length of the spin wave (at least an order of magnitude longer than the wavelength). Thus the YIG-based magnonic bends could be realized as an effective tool to connect the magnonic units together. The proposed scheme of the consequent magnonic bends supports the spin-wave mode transformation regime due to the intrinsic confinement of the waveguide sections, which could be useful to perform the spin-wave interference, which is mainly responsible for the wave logic operation.

IX. CONCLUSION

In conclusion, using both experimental methods and micromagnetic modeling, we show that the in-plane magnonic bend can serve as a useful tool not only for connecting functional magnonic elements but also providing for both frequency filtering and wavelength conversion. Our experimental results show that the fabricated in-plane and out-of-plane bends can be simulated well using micromagnetic simulations. The proposed $45°$ bend is most promising for multimode magnonics because of the simple structuring, design, and fabrication as well as the optimum signal transmission for SWs propagating along an in-plane bend.

We also demonstrate, using micromagnetic simulations, that effective transmission of SW signals can be achieved across a three-dimensional structure formed by two right-angled bends. The proposed structure with two bends (lateral and vertical) allows for both spatial frequency selection and wavelength conversion of spin-wave signals, rendering it possible to serve not just as a spin-wave conduit but as a functional element in multilayer information processing systems. The signal transmission between layers of a magnonic device allows one to fabricate complex devices based on magnonic logic with a large number of functional elements per unit length.

The data that support the findings of this study are available from the corresponding author upon reasonable request.

APPENDIX

For the case of exciting the MSSW in the input arm of the L-shaped waveguide, a reduction in the width of the waveguide leads to an increasing overlap of the frequency ranges of the MSSW and the BVMSW. The efficiency of excitation of the MSSW in the output arm of the L-shaped waveguide will therefore be determined by the frequency dependence of the overlap integral $\Sigma(f)$ between the high-frequency magnetic field $h_1(y,f)$ generated by the MSSW and the magnetization profile $m_2(y,f)$ of the SW in the BVMSW configuration in the direction across the film thickness:

$$\Sigma(f) = \int_{-\infty}^{\infty} \vec{h}_1 \cdot \vec{m}_2 \, dy$$

$$= \int_{-\infty}^{\infty} \nabla\psi_1(y,f) \cdot \hat{\chi} \cdot \nabla\psi_2(y,f) \, dy,$$

where $\hat{\chi}$ is the corresponding magnetic susceptibility tensor, and $\psi_1(y,f)$ and $\psi_2(y,f)$ are the magnetostatic potential for the MSSWs and BVMSWs at the frequency f.

The potential functions for MSSWs (ψ_1) and BVMSWs (ψ_2) in each region can be written as follows [52]:

$$\psi_1 = \begin{cases} \psi_0(e^{kd} + pe^{-ky+ikx}, y > d/2 \\ \psi_0(e^{ky} + pe^{-ky})e^{ikx}, y \geq d/2 \\ \psi_0(1 + pe^{kd})e^{ky+ikx}, y < -d/2; \end{cases}$$

$$\psi_2 = \begin{cases} \psi_0 e^{k_z d/2}\cos(k_y d/2)e^{ik_z-k_z y}, y > d/2 \\ \psi_0 \cos(k_y y)e^{ik_z}, |y| \geq d/2 \\ \psi_0 e^{k_z d/2}\cos(k_y d/2)e^{ik_z+k_z y}, y < -d/2, \end{cases}$$

where ψ_0 is an arbitrary constant determining the mode amplitude, $p = \chi - k/\chi + 2 - ke^{-kd}$, $\chi = \omega_0\omega_M/\omega_0^2 - \omega^2$ is the magnetic susceptibility, $\omega_M = -\gamma\mu_0 M_s$, and $\omega_0 = -\gamma\mu_0 H_0$.

Figure 11(a) shows the potential functions for the lowest-order even BVMSW and MSSW modes. The wave amplitude of the MSSW decays exponentially from the surfaces of the film, while for BVMSW the zero value of ψ_2 is located in the center of the film. The result of the numerical computation of the overlap integral (Fig. 11)
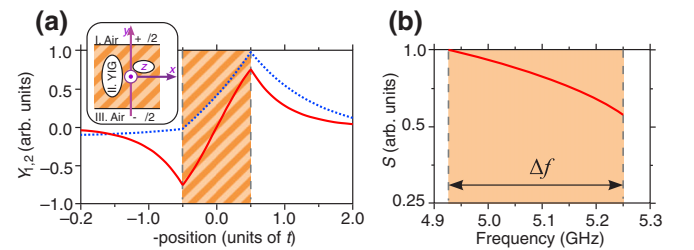

FIG. 11. (a) Potential profile for the lowest-order even backward volume wave modes (solid curve) and for surface wave (dashed curve) at the frequency $f = 5$ GHz. (b) Frequency dependence of the value of overlap integral of BVMSW and MSSW potential functions. All data are presented for $H_0 = 1200$ Oe.

for the YIG waveguide with width 500 μm and thickness 10 μm demonstrates that the value of the normalized Σ is reduced by a factor of 1.75 when the frequency is increased in the frequency range Δf (where there is coexistence of MSSWs and BVMSWs).

———————

[1] V. V. Kruglyak, S. O. Demokritov, and D. Grundler, Magnonics, J. Phys. D: Appl. Phys. **43,** 264001 (2010).

[2] A. Barman, *et al.*, The 2021 magnonics roadmap, J. Phys.: Condens. Matter **33,** 413001 (2021).

[3] A. V. Chumak, *et al.*, Advances in magnetics roadmap on spin-wave computing (2022).

[4] A. V. Sadovnikov, C. S. Davies, S. V. Grishin, V. V. Kruglyak, D. V. Romanenko, Y. P. Sharaevskii, and S. A. Nikitov, Magnonic beam splitter: The building block of parallel magnonic circuitry, Appl. Phys. Lett. **106,** 192406 (2015).

[5] R. Perricone, X. S. Hu, J. Nahas, and M. Niemier, Design of 3d nanomagnetic logic circuits: A full-adder case study, Design, Automation & Test in Europe Conference & Exhibition, 2014.

[6] A. Khitun, M. Bao, and K. L. Wang, Magnonic logic circuits, J. Phys. D: Appl. Phys. **43,** 264005 (2010).

[7] Y. Au, M. Dvornik, O. Dmytriiev, and V. V. Kruglyak, Nanoscale spin wave valve and phase shifter, Appl. Phys. Lett. **100,** 172408 (2012).

[8] A. V. Sadovnikov, E. N. Beginin, S. E. Sheshukova, D. V. Romanenko, Y. P. Sharaevsky, and S. A. Nikitov, Directional multimode coupler for planar magnonics: Side-coupled magnetic stripes, Appl. Phys. Lett. **107,** 202405 (2015).

[9] Q. Wang, M. Kewenig, M. Schneider, R. Verba, F. Kohl, B. Heinz, M. Geilen, M. Mohseni, B. Lägel, F. Ciubotaru, C. Adelmann, C. Dubs, S. D. Cotofana, O. V. Dobrovolskiy, T. Brächer, P. Pirro, and A. V. Chumak, A magnonic directional coupler for integrated magnonic half-adders, Nat. Electron. **3,** 765 (2020).

[10] G. Csaba, Á. Papp, and W. Porod, Perspectives of using spin waves for computing and signal processing, Phys. Lett. A **381,** 1471 (2017).

[11] M. P. Kostylev, A. A. Serga, T. Schneider, B. Leven, and B. Hillebrands, Spin-wave logical gates, Appl. Phys. Lett. **87,** 153501 (2005).

[12] K.-S. Lee and S.-K. Kim, Conceptual design of spin wave logic gates based on a Mach–Zehnder-type spin wave interferometer for universal logic functions, J. Appl. Phys. **104,** 053909 (2008).

[13] T. Schneider, A. A. Serga, B. Leven, B. Hillebrands, R. L. Stamps, and M. P. Kostylev, Realization of spin-wave logic gates, Appl. Phys. Lett. **92,** 022505 (2008).

[14] A. Imre, Majority logic gate for magnetic quantum-dot cellular automata, Science **311,** 205 (2006).

[15] M. T. Niemier, G. H. Bernstein, G. Csaba, A. Dingler, X. S. Hu, S. Kurtz, S. Liu, J. Nahas, W. Porod, M. Siddiq, and E. Varga, Nanomagnet logic: Progress toward system-level integration, J. Phys.: Condens. Matter **23,** 493202 (2011).

[16] A. V. Sadovnikov, E. N. Beginin, S. E. Sheshukova, Y. P. Sharaevskii, A. I. Stognij, N. N. Novitski, V. K. Sakharov, Y. V. Khivintsev, and S. A. Nikitov, Route toward semiconductor magnonics: Light-induced spin-wave nonreciprocity in a YIG/GaAs structure, Phys. Rev. B **99,** 054424 (2019).

[17] V. E. Demidov, S. Urazhdin, A. Anane, V. Cros, and S. O. Demokritov, Spin–orbit-torque magnonics, J. Appl. Phys. **127,** 170901 (2020).

[18] N. Thiery, V. V. Naletov, L. Vila, A. Marty, A. Brenac, J.-F. Jacquot, G. de Loubens, M. Viret, A. Anane, V. Cros, J. B. Youssef, N. Beaulieu, V. E. Demidov, B. Divinskiy, S. O. Demokritov, and O. Klein, Electrical properties of epitaxial yttrium iron garnet ultrathin films at high temperatures, Phys. Rev. B **97,** 064422 (2018).

[19] Y. V. Khivintsev, V. K. Sakharov, S. L. Vysotskii, Y. A. Filimonov, A. I. Stognii, and S. A. Nikitov, Magnetoelastic waves in submicron yttrium–iron garnet films manufactured by means of ion-beam sputtering onto gadolinium–gallium garnet substrates, Techn. Phys. **63,** 1029 (2018).

[20] A. V. Chumak, V. I. Vasyuchka, A. A. Serga, and B. Hillebrands, Magnon spintronics, Nat. Phys. **11,** 453 (2015).

[21] M. Dvornik and V. V. Kruglyak, Dispersion of collective magnonic modes in stacks of nanoscale magnetic elements, Phys. Rev. B **84,** 140405(R) (2011).

[22] S. Thompson, MOS scaling: Transistor challenges for the 21st century, Intel Technol. J. (1998).

[23] J. Kiermaier, S. Breitkreutz, G. Csaba, D. Schmitt-Landsiedel, and M. Becherer, Electrical input structures for nanomagnetic logic devices, J. Appl. Phys. **111,** 07E341 (2012).

[24] S. Liu, X. S. Hu, M. T. Niemier, J. J. Nahas, G. Csaba, G. H. Bernstein, and W. Porod, Exploring the design of the magnetic–electrical interface for nanomagnet logic, IEEE Trans. Nanotechnol. **12,** 203 (2013).

[25] A. I. Stognij, L. V. Lutsev, V. E. Bursian, and N. N. Novitskii, Growth and spin-wave properties of thin $Y_3Fe_5O_{12}$ films on Si substrates, J. Appl. Phys. **118,** 023905 (2015).

[26] G. Gubbiotti, A. Sadovnikov, E. Beginin, S. Nikitov, D. Wan, A. Gupta, S. Kundu, G. Talmelli, R. Carpenter, I. Asselberghs, I. P. Radu, C. Adelmann, and F. Ciubotaru, Magnonic Band Structure in Vertical Meander-Shaped $Co_{40}Fe_{40}B_{20}$ Thin Films, Phys. Rev. Appl. **15,** 014061 (2021).

[27] G. Gubbiotti, A. Sadovnikov, E. Beginin, S. Sheshukova, S. Nikitov, G. Talmelli, I. Asselberghs, I. P. Radu, C. Adelmann, and F. Ciubotaru, Magnonic band structure in CoFeB/Ta/NiFe meander-shaped magnetic bilayers, Appl. Phys. Lett. **118,** 162405 (2021).

[28] I. Turčan, L. Flajšman, O. Wojewoda, V. Roučka, O. Man, and M. Urbánek, Spin wave propagation in corrugated waveguides, Appl. Phys. Lett. **118,** 092405 (2021).

[29] V. K. Sakharov, E. N. Beginin, Y. V. Khivintsev, A. V. Sadovnikov, A. I. Stognij, Y. A. Filimonov, and S. A. Nikitov, Spin waves in meander shaped YIG film: Toward 3D magnonics, Appl. Phys. Lett. **117,** 022403 (2020).

[30] V. Sakharov, Y. Khivintsev, S. Vysotskii, A. Stognij, Y. Filimonov, A. Sadovnikov, E. Beginin, and S. Nikitov, Spin wave filtration by resonances in the sidewalls of corrugated yttrium-iron garnet films, J. Magn. Magn. Mater. **545,** 168786 (2022).

[31] P. Clausen, K. Vogt, H. Schultheiss, S. Schäfer, B. Obry, G. Wolf, P. Pirro, B. Leven, and B. Hillebrands, Mode

conversion by symmetry breaking of propagating spin waves, Appl. Phys. Lett. **99**, 162505 (2011).

[32] K. Vogt, H. Schultheiss, S. Jain, J. E. Pearson, A. Hoffmann, S. D. Bader, and B. Hillebrands, Spin waves turning a corner, Appl. Phys. Lett. **101**, 042410 (2012).

[33] V. S. Tkachenko, A. N. Kuchko, M. Dvornik, and V. V. Kruglyak, Propagation and scattering of spin waves in curved magnonic waveguides, Appl. Phys. Lett. **101**, 152402 (2012).

[34] T. Brächer, P. Pirro, J. Westermann, T. Sebastian, B. Lägel, B. Van de Wiele, A. Vansteenkiste, and B. Hillebrands, Generation of propagating backward volume spin waves by phase-sensitive mode conversion in two-dimensional microstructures, Appl. Phys. Lett. **102**, 132411 (2013).

[35] A. V. Sadovnikov, C. S. Davies, V. V. Kruglyak, D. V. Romanenko, S. V. Grishin, E. N. Beginin, Y. P. Sharaevskii, and S. A. Nikitov, Spin wave propagation in a uniformly biased curved magnonic waveguide, Phys. Rev. B **96**, 060401(R) (2017).

[36] CJSC NII Materialovedenie, Zelenograd, Russia.

[37] A. Vansteenkiste, J. Leliaert, M. Dvornik, M. Helsen, F. Garcia-Sanchez, and B. Waeyenberge, The design and verification of MuMax3, AIP Adv. **4**, 107133 (2014).

[38] L. D. Landau and E. M. Lifschitz, On the theory of the dispersion of magnetic permeability in ferromagnetic bodies, Phys. Z. Sowjet. **8**, 153 (1935).

[39] I. V. Zavislyak and A. V. Tychinskii, *Physical Principles of Functional Microelectronics* (UMK VO, 1989).

[40] T. Gilbert, A Lagrangian formulation of the gyromagnetic equation of the magnetization field, Phys. Rev. **100**, 1243 (1955).

[41] J. Dormand and P. Prince, A family of embedded Runge-Kutta formulae, J. Comput. Appl. Math. **6**, 19 (1980).

[42] A. V. Sadovnikov, A. A. Grachev, E. N. Beginin, S. E. Sheshukova, Y. P. Sharaevskii, and S. A. Nikitov, Voltage-Controlled Spin-Wave Coupling in Adjacent Ferromagnetic-Ferroelectric Heterostructures, Phys. Rev. Appl. **7**, 014013 (2017).

[43] A. V. Sadovnikov, A. A. Grachev, S. E. Sheshukova, Y. P. Sharaevskii, A. A. Serdobintsev, D. M. Mitin, and S. A. Nikitov, Magnon Straintronics: Reconfigurable Spin-Wave Routing in Strain-Controlled Bilateral Magnetic Stripes, Phys. Rev. Lett. **120**, 257203 (2018).

[44] G. Venkat, H. Fangohr, and A. Prabhakar, Absorbing boundary layers for spin wave micromagnetics, J. Magn. Magn. Mater. **450**, 34 (2018).

[45] M. Dvornik, A. N. Kuchko, and V. V. Kruglyak, Micromagnetic method of s-parameter characterization of magnonic devices, J. Appl. Phys. **109**, 07D350 (2011).

[46] A. A. Serga, A. V. Chumak, and B. Hillebrands, YIG magnonics, J. Phys. D: Appl. Phys. **43**, 264002 (2010).

[47] R. Damon and J. Eschbach, Magnetostatic modes of a ferromagnet slab, J. Phys. Chem. Solids **19**, 308 (1961).

[48] T. W. O'Keeffe and R. W. Patterson, Magnetostatic surface-wave propagation in finite samples, J. Appl. Phys. **49**, 4886 (1978).

[49] S. Demokritov, Brillouin light scattering studies of confined spin waves: Linear and nonlinear confinement, Phys. Rep. **348**, 441 (2001).

[50] A. G. Gurevich and G. A. Melkov, *Magnetization Oscillations and Waves* (CRC-Press, London, New York, 1996).

[51] S. N. Bajpai, Excitation of magnetostatic surface waves: Effect of finite sample width, J. Appl. Phys. **58**, 910 (1985).

[52] D. D. Stancil and A. Prabhakar, *Spin Waves: Theory and Applications* (Springer, New York, 2009).

[53] O. Karlqvist, Calculation of the magnetic field in the ferromagnetic layer of a magnetic drum, Trans. Roy. Inst. Technol. **86**, 00 (1954).

[54] B. A. Kalinikos and A. N. Slavin, Theory of dipole-exchange spin wave spectrum for ferromagnetic films with mixed exchange boundary conditions, J. Phys. C: Solid State Phys. **19**, 7013 (1986).

[55] A. V. Vashkovskii, V. S. Stalmakhov, and Y. P. Sharaevskii, *Magnetostatic Waves in Microwave Electronics* (Sarat. Gos. Univ. (in Russian), 1993).

[56] O. Buttner, M. Bauer, C. Mathieu, S. O. Demokritov, B. Hillebrands, P. A. Kolodin, M. P. Kostylev, S. Sure, H. Dotsch, V. Grimalsky, Y. Rapoport, and A. N. Slavin, Mode beating of spin wave beams in ferrimagnetic $Lu_{2.04}Bi_{0.96}Fe_5O_{12}$ films, IEEE Trans. Magn. **34**, 1381 (1998).

[57] V. S. L'vo, in *Wave Turbulence Under Parametric Excitation: Applications to Magnets* (Springer Berlin Heidelberg, Berlin, Heidelberg, 1994), p. 95.

[58] S. O. Demokritov, B. Hillebrands, and A. N. Slavin, Brillouin light scattering studies of confined spin waves: Linear and nonlinear confinement, Phys. Rep. **348**, 441 (2001).

[59] J. Jorzick, C. Krämer, S. O. Demokritov, B. Hillebrands, B. Bartenlian, C. Chappert, D. Decanini, F. Rousseaux, E. Cambril, E. Sondergard, M. Bailleul, C. Fermon, and A. N. Slavin, Spin wave quantization in laterally confined magnetic structures (invited), J. Appl. Phys. **89**, 7091 (2001).

[60] V. E. Demidov, S. O. Demokritov, K. Rott, P. Krzysteczko, and G. Reiss, Self-focusing of spin waves in permalloy microstripes, Appl. Phys. Lett. **91**, 252504 (2007).

[61] V. E. Demidov, S. O. Demokritov, K. Rott, P. Krzysteczko, and G. Reiss, Linear and nonlinear spin-wave dynamics in macro- and microscopic magnetic confined structures, J. Phys. D: Appl. Phys. **41**, 164012 (2008).

[62] A. V. Sadovnikov, A. A. Grachev, V. A. Gubanov, S. A. Odintsov, A. A. Martyshkin, S. E. Sheshukova, Y. P. Sharaevskii, and S. A. Nikitov, Spin-wave intermodal coupling in the interconnection of magnonic units, Appl. Phys. Lett. **112**, 142402 (2018).

[63] C. S. Davies, V. D. Poimanov, and V. V. Kruglyak, Mapping the magnonic landscape in patterned magnetic structures, Phys. Rev. B **96**, 094430 (2017).

[64] K. Vogt, F. Fradin, J. Pearson, T. Sebastian, S. Bader, B. Hillebrands, A. Hoffmann, and H. Schultheiss, Realization of a spin-wave multiplexer, Nat. Commun. **5**, 3727 (2014).

[65] T. Schneider, A. A. Serga, A. V. Chumak, C. W. Sandweg, S. Trudel, S. Wolff, M. P. Kostylev, V. S. Tiberkevich, A. N. Slavin, and B. Hillebrands, Nondiffractive Subwavelength Wave Beams in a Medium with Externally Controlled Anisotropy, Phys. Rev. Lett. **104**, 197203 (2010).

[66] A. V. Vashkovsky and E. H. Lock, Properties of backward electromagnetic waves and negative reflection in ferrite films, Phys.-Usp. **49**, 389 (2006).

[67] E. H. Lock, The properties of isofrequency dependences and the laws of geometrical optics, Phys.-Usp. **51**, 375 (2008).

[68] R. Gieniusz, H. Ulrichs, V. D. Bessonov, U. Guzowska, A. I. Stognii, and A. Maziewski, Single antidot as a passive way to create caustic spin-wave beams in yttrium iron garnet films, Appl. Phys. Lett. **102,** 102409 (2013).

[69] C. S. Davies, A. V. Sadovnikov, S. V. Grishin, Y. P. Sharaevskii, S. A. Nikitov, and V. V. Kruglyak, Generation of propagating spin waves from regions of increased dynamic demagnetising field near magnetic antidots, Appl. Phys. Lett. **107,** 162401 (2015).

[70] A. Y. Annenkov, S. V. Gerus, and E. H. Lock, Superdirectional beam of surface spin wave, Europhys. Lett. **123,** 44003 (2018).

[71] T. Sebastian, K. Schultheiss, B. Obry, B. Hillebrands, and H. Schultheiss, Micro-focused Brillouin light scattering: Imaging spin waves at the nanoscale, Front. Phys. **3,** 35 (2015).

[72] C. S. Davies, A. V. Sadovnikov, S. V. Grishin, Y. P. Sharaevsky, S. A. Nikitov, and V. V. Kruglyak, Field-Controlled Phase-Rectified Magnonic Multiplexer, IEEE Trans. Magn. **51,** 3401904 (2015).

[73] S. L. Vysotskii, A. V. Sadovnikov, G. M. Dudko, A. V. Kozhevnikov, Y. V. Khivintsev, V. K. Sakharov, N. N. Novitskii, A. I. Stognij, and Y. A. Filimonov, Spin-wave generation at the thickness step of yttrium iron garnet film, Appl. Phys. Lett. **117,** 102403 (2020).

[74] E. N. Beginin, A. V. Sadovnikov, A. Y. Sharaevskaya, A. I. Stognij, and S. A. Nikitov, Spin wave steering in three-dimensional magnonic networks, Appl. Phys. Lett. **112,** 122404 (2018).

[75] D. Grundler, Nanomagnonics around the corner, Nat. Nanotech. **11,** 407 (2016).

[76] S. R. Lake, B. Divinskiy, G. Schmidt, S. O. Demokritov, and V. E. Demidov, Interplay Between Nonlinear Spectral Shift and Nonlinear Damping of Spin Waves in Ultrathin Yttrium Iron Garnet Waveguides, Phys. Rev. Appl. **17,** 034010 (2022).

[77] M. Collet, O. Gladii, M. Evelt, V. Bessonov, L. Soumah, P. Bortolotti, S. O. Demokritov, Y. Henry, V. Cros, M. Bailleul, V. E. Demidov, and A. Anane, Spin-wave propagation in ultra-thin YIG based waveguides, Appl. Phys. Lett. **110,** 092408 (2017).

[78] Q. Wang, P. Pirro, R. Verba, A. Slavin, B. Hillebrands, and A. V. Chumak, Reconfigurable nanoscale spin-wave directional coupler, Sci. Adv. **4,** e1701517 (2018).

[79] Q. Wang, B. Heinz, R. Verba, M. Kewenig, P. Pirro, M. Schneider, T. Meyer, B. Lägel, C. Dubs, T. Brächer, and A. V. Chumak, Spin Pinning and Spin-Wave Dispersion in Nanoscopic Ferromagnetic Waveguides, Phys. Rev. Lett. **122,** 247202 (2019).

[80] H. Merbouche, M. Collet, M. Evelt, V. E. Demidov, J. L. Prieto, M. Muñoz, J. Ben Youssef, G. de Loubens, O. Klein, S. Xavier, O. D'Allivy Kelly, P. Bortolotti, V. Cros, A. Anane, and S. O. Demokritov, Frequency filtering with a magnonic crystal based on nanometer-thick yttrium iron garnet films, ACS Appl. Nano Mater. **4,** 121 (2021).

[81] Y. Khivintsev, V. Sakharov, A. Kozhevnikov, G. Dudko, Y. Filimonov, and A. Khitun, Spin waves in YIG based magnonic networks: Design and technological aspects, J. Magn. Magn. Mater. **545,** 168754 (2022).

[82] B. Divinskiy, H. Merbouche, K. Nikolaev, S. Michaelis de Vasconcellos, R. Bratschitsch, D. Gouéré, R. Lebrun, V. Cros, J. Ben Youssef, P. Bortolotti, A. Anane, S. Demokritov, and V. Demidov, Dispersionless Propagation of Ultrashort Spin-Wave Pulses in Ultrathin Yttrium Iron Garnet Waveguides, Phys. Rev. Appl. **16,** 024028 (2021).

[83] Q. Wang, B. Heinz, R. Verba, M. Kewenig, P. Pirro, M. Schneider, T. Meyer, B. Lägel, C. Dubs, T. Brächer, and A. Chumak, Spin Pinning and Spin-Wave Dispersion in Nanoscopic Ferromagnetic Waveguides, Phys. Rev. Lett. **122,** 247202 (2019).

[84] A. I. Akhiezer, V. G. Bar'yakhtar, and S. V. Peletminskii, *Spin Waves* (Nauka, Moscow, 1967).

[85] K. Y. Guslienko, S. O. Demokritov, B. Hillebrands, and A. N. Slavin, Effective dipolar boundary conditions for dynamic magnetization in thin magnetic stripes, Phys. Rev. B **66,** 132402 (2002).

[86] K. Y. Guslienko and A. N. Slavin, Boundary conditions for magnetization in magnetic nanoelements, Phys. Rev. B **72,** 014463 (2005).

[87] V. E. Demidov, S. Urazhdin, A. Zholud, A. V. Sadovnikov, and S. O. Demokritov, Dipolar field-induced spin-wave waveguides for spin-torque magnonics, Appl. Phys. Lett. **106,** 022403 (2015).

[88] A. Serga, A. Andre, S. Demokritov, B. Hillebrands, and A. Slavin, Black soliton formation from phase-adjusted spin wave packets, J. Appl. Phys. **95,** 6607 (2004).

[89] A. B. Ustinov, B. A. Kalinikos, V. E. Demidov, and S. O. Demokritov, Formation of gap solitons in ferromagnetic films with a periodic metal grating, Phys. Rev. B **81,** 180406 (2010).

[90] M. P. Kostylev, A. A. Serga, T. Schneider, B. Leven, and B. Hillebrands, Spin-wave logical gates, Appl. Phys. Lett. **87,** 153501 (2005).

[91] N. Kanazawa, T. Goto, K. Sekiguchi, A. B. Granovsky, C. A. Ross, H. Takagi, Y. Nakamura, and M. Inoue, Demonstration of a robust magnonic spin wave interferometer, Sci. Rep. **6,** 1 (2016).

[92] N. Sato, K. Sekiguchi, and Y. Nozaki, Electrical demonstration of spin-wave logic operation, Appl. Phys. Exp. **6,** 063001 (2013).

[93] N. Kanazawa, T. Goto, K. Sekiguchi, A. Granovsky, C. Ross, H. Takagi, Y. Nakamura, H. Uchida, and M. Inoue, The role of Snell's law for a magnonic majority gate, Sci. Rep. **7,** 7898 (2017).

[94] T. Fischer, M. Kewenig, D. Bozhko, A. Serga, I. Syvorotka, F. Ciubotaru, C. Adelmann, B. Hillebrands, and A. Chumak, Experimental prototype of a spin-wave majority gate, Appl. Phys. Lett. **110,** 152401 (2017).